

# Spectroscopic evidence for negative electronic compressibility in a quasi-three-dimensional spin-orbit correlated metal

Junfeng He<sup>1\*</sup>, T. Hogan<sup>1\*</sup>, Thomas R. Mion<sup>1</sup>, H. Hafiz<sup>2</sup>, Y. He<sup>3</sup>, S.-K. Mo<sup>4</sup>, C. Dhital<sup>1</sup>, X. Chen<sup>1</sup>, Qisen Lin<sup>1</sup>, Y. Zhang<sup>5</sup>, M. Hashimoto<sup>3</sup>, H. Pan<sup>1</sup>, D. H. Lu<sup>3</sup>, M. Arita<sup>6</sup>, K. Shimada<sup>6</sup>, R. S. Markiewicz<sup>2</sup>, Z. Wang<sup>1</sup>, K. Kempa<sup>1</sup>, M. J. Naughton<sup>1</sup>, A. Bansil<sup>2</sup>, S. D. Wilson<sup>1,7</sup>, and Rui-Hua He<sup>1</sup>

<sup>1</sup>*Department of Physics, Boston College, Chestnut Hill, MA 02467, USA*

<sup>2</sup>*Physics Department, Northeastern University, Boston, MA 02115, USA*

<sup>3</sup>*Stanford Synchrotron Radiation Lightsource and  
Stanford Institute for Materials and Energy Sciences,*

*SLAC National Accelerator Laboratory, Menlo Park, CA 94025, USA*

<sup>4</sup>*Advanced Light Source, Lawrence Berkeley National Laboratory, Berkeley, CA 94720, USA*

<sup>5</sup>*International Center for Quantum Materials,  
Peking University, Beijing 100871, China*

<sup>6</sup>*Hiroshima Synchrotron Radiation Center,  
Hiroshima University, Hiroshima 739-0046, Japan*

<sup>7</sup>*Materials Department, University of California, Santa Barbara, CA 93106, USA*

---

\* These authors contributed equally to this work.

## Abstract

Negative compressibility is a sign of thermodynamic instability and can only be found in open [1–3] or nonequilibrium [4, 5] systems. However, in quantum materials consisting of multiple mutually-coupled subsystems, the effective compressibility of one subsystem can be negative which is countered by the positive compressibility of other subsystems. Manifestations of such negative compressibility in quantum materials have so far been limited to low-dimensional dilute electron systems [6–11]. Their origins have been commonly attributed to a dominance of the exchange energy over kinetic energy of electrons, although other routes to negative electronic compressibility have been conceived in theory [12]. Here we present evidence from angle-resolved photoemission spectroscopy (ARPES) for negative electronic compressibility in a quasi three-dimensional (3D) spin-orbit correlated metal,  $(\text{Sr}_{1-x}\text{La}_x)_3\text{Ir}_2\text{O}_7$ , which is driven by a dominance of the correlation energy of electrons at a relatively high density. Increased electron filling results in both an expansion of the electron Fermi pockets and an anomalous decrease of the chemical potential. This anomaly, suggestive of negative electronic compressibility, is made possible by a concomitant rapid lowering in energy of the correlated conduction band on which the chemical potential is defined, unveiling a new band picture of doping Mott insulators. Our finding points to a distinct pathway toward an uncharted territory of negative electronic compressibility which potentially features a variety of bulk correlated metals [13] with unique prospective applications in low-power nanoelectronics and novel metamaterials.

Understanding the ground-state property of an electron system requires information about its single-particle band structure as well as many-body effects. Both pieces of information are contained in a fundamental thermodynamic quantity—the electronic compressibility, which is defined as  $\kappa_e = \frac{1}{n^2} \frac{\partial n}{\partial \mu}$ , where  $n$  is the carrier density,  $\mu$  is the chemical potential. Such information is experimentally accessible, e.g., from ARPES, which provides independent measures of  $n$  and the change in  $\mu$  [14], as we shall demonstrate in the following.

$\text{Sr}_3\text{Ir}_2\text{O}_7$  is an insulator driven by a cooperative interplay between correlation effects and strong spin-orbit coupling of the Ir  $5d$  electrons [15–18]. It crystallizes in a near tetragonal structure containing two  $\text{IrO}_2$  planes per unit cell, with the corresponding in-plane Brillouin zone (BZ) indicated by the white dashed line in Fig. 1a [19–22].  $\text{Sr}_3\text{Ir}_2\text{O}_7$  has a significantly stronger three dimensionality with the c-axis and in-plane resistivity only differing by  $\sim 4$  times, compared to cuprates which have a difference of 2 to 4 orders of magnitude [19]. Substituting one Sr atom with La effectively dopes one electron into the system, which leads to an insulator-metal transition at  $x \sim 0.033$  in  $(\text{Sr}_{1-x}\text{La}_x)_3\text{Ir}_2\text{O}_7$  [19]. Our ARPES experiment shows that the doped electrons initially populate the conduction band from its bottoms near M points, forming four apparent electron pockets at  $\mu$  in each BZ (Fig. 1a). The number, momentum location, overall shape of the observed pockets and associated band dispersions, agree well with the first-principles calculations (cf. Fig. 1a-e). As  $x$  increases, electron pockets expand in momentum, as indicated by an increasing separation between two given Fermi momenta on the pocket (Fig. 1b & f). Both  $n$  and the effective La substitution level  $x_{\text{ARPES}}$  can be estimated for each measured sample based on the four pockets’ area percentage in the BZ and known lattice constants [23].  $x_{\text{ARPES}}$  agrees well within error bars with the La substitution level measured using energy-dispersive x-ray spectroscopy (EDX) on the same sample (Fig. 1g).

A traditional means to determine the change in  $\mu$  by photoemission is to study the energy shift of core levels, which suffers from a poor experimental resolution and complications by other contributing factors aside from the change in  $\mu$  itself [14] (see Supplementary Discussion 1 for elaboration). A more accurate and straightforward approach is to study some low-binding-energy ( $\leq 6$  eV) yet fully-occupied valence-band orbitals, which has been demonstrated in the case of a hole-doped cuprate [24] and yielded results consistent with the core-level approach [25]. Energy shifts of these delocalized (Fig. 2a) band-like orbitals can simply represent the change in  $\mu$  because effects due to other site-dependent

and/or local factors are averaged out (see Supplementary Discussion 1). Our observation in  $(\text{Sr}_{1-x}\text{La}_x)_3\text{Ir}_2\text{O}_7$  is consistent with this valence-band approach where the general shape of the (deep) valence-band spectra remain qualitatively unchanged with doping, apart from this shift (Fig. 2a-d). As  $x$  increases, we see that, e.g. in Fig. 2d, the O  $2p$  orbital at X point [21] systematically decreases its energy relative to the respective  $\mu$ , revealing in turn a decrease of  $\mu$ . A similar behavior was found on different states, such as those around  $\Gamma$  of a mixed Ir-O character displaying an unambiguous overall upward band shift (Fig. 2a-c). Relative shifts of  $\mu$  deduced from those of various deep valence-band states are summarized in Fig. 2e, which consistently depict a systematic decrease of  $\mu$  with increased electron filling. This trend is in overall agreement with the limited results obtained from the core-level approach, considering the aforementioned caveats thereof (Supplementary Fig. S2 and see Supplementary Discussion 1).

In a rigid-band picture, all energy bands shift equally while maintaining their separations, thus an electron filling increase necessarily leads to an increase of  $\mu$ . We found the anomalous behavior of  $\mu$  in metallic  $(\text{Sr}_{1-x}\text{La}_x)_3\text{Ir}_2\text{O}_7$  accompany nontrivial motions of the conduction and valence bands at the lowest binding energy. Upon the increase of electron filling, the conduction band bottom at M point sinks deeper under  $\mu$  (Fig. 3c), while the valence band top at X point rises (Fig. 3a & b), resulting in a decrease of their (indirect) bandgap (Fig. 3d). Their motions are, nevertheless, highly asymmetric, as suggested by Fig. 4a that has combined the doping dependence information of both the  $\mu$  shift (Fig. 2e) and the conduction-valence band motion. The conduction band bottom continuously decreases its referenced energy (by  $\sim 100$  meV) as  $x$  increases from 0.035 to 0.086, whereas the apparent valence band top exhibits an abrupt increase in energy (by  $\sim 150$  meV) across  $x \sim 0.05$ , and an otherwise moderate (if any beyond the error bars) shift away from this doping region. This abrupt variation indicates a character change of the dominant states defining the apparent valence band top. The observed spectral evolution across  $x \sim 0.05$  is consistent with a spectral weight transfer from the original valence-band states to some states newly appearing at lower energy inside the original bandgap (Fig. 4b). This type of spectral weight transfer was found typical in electron-doped transition-metal oxides [13], including  $\text{Sr}_{2-x}\text{La}_x\text{IrO}_4$  [26].

The observed dramatic bandgap reduction, appearance of in-gap states, and spectral weight transfer over a wide energy range, all upon moderate electron doping, point to the

correlated nature of the low-lying states close to  $\mu$ . This overall situation is similar to the electron-doped cuprates,  $\text{Nd}_{2-x}\text{Ce}_x\text{CuO}_4$  [27] (cf. Fig. 4c & d); in which the bandgap between the lowest-lying (in-gap) valence band and conduction band is understood as due to antiferromagnetic correlations, and the higher energy (original) valence band is a remnant of the lower Hubbard band [27, 28]. Whether or not the bandgap in metallic  $(\text{Sr}_{1-x}\text{La}_x)_3\text{Ir}_2\text{O}_7$  is similarly magnetic in nature, we note the  $J = 1/2$  antiferromagnetic correlations at  $x = 0$ , driven by on-site Coulomb repulsion and spin-orbit coupling [15–18], were recently found to persist over a short range in the metallic regime and weaken with increasing doping (S. D. Wilson, private communication), similar to  $\text{Nd}_{2-x}\text{Ce}_x\text{CuO}_4$  [27].

However, a mere reduction of the correlation gap is not sufficient to understand the counterintuitive  $\mu$  shift observed in  $(\text{Sr}_{1-x}\text{La}_x)_3\text{Ir}_2\text{O}_7$ , as  $\mu$  was found in  $\text{Nd}_{2-x}\text{Ce}_x\text{CuO}_4$  to shift in the normal way [14, 27] (cf. Fig. 4c & d). Another essential aspect is the manner in which the bandgap reduces. In general,  $\mu$  tends to move up in energy relative to the conduction band bottom in accordance with the increase of electron filling, while it is largely insensitive to the motion and variation in the valence band as long as it stays occupied. But in  $(\text{Sr}_{1-x}\text{La}_x)_3\text{Ir}_2\text{O}_7$ , the conduction band bottom itself moves down more rapidly as the bandgap shrinks, resulting in an effective lowering of  $\mu$ . In  $\text{Nd}_{2-x}\text{Ce}_x\text{CuO}_4$ , as a contrast, the conduction band bottom barely moves with  $x$ . Instead, the valence band top moves drastically upward, and once it reaches above  $\mu$ , its further elevation tends to drive  $\mu$  up due to its hole-like nature.

Therefore, the unique correlation gap evolution holds the key to understanding the observed anomalous  $\mu$  shift in  $(\text{Sr}_{1-x}\text{La}_x)_3\text{Ir}_2\text{O}_7$ . Several microscopic aspects may contribute to make the  $(\text{Sr}_{1-x}\text{La}_x)_3\text{Ir}_2\text{O}_7$  case distinct from  $\text{Nd}_{2-x}\text{Ce}_x\text{CuO}_4$ . As a result of a negative  $\frac{\partial n}{\partial \mu}$ , local electron density fluctuations promote the tendency toward electronic phase separation, which would be frustrated by the long-range Coulomb interaction and then confined to a microscopic scale. While in-gap states can exist in systems without microscopic phase separation (e.g., in  $\text{Nd}_{2-x}\text{Ce}_x\text{CuO}_4$  [27]), both were found in  $\text{La}_{2-x}\text{Sr}_x\text{CuO}_4$  and may be related to a doping independence of  $\mu$  observed in a certain doping range [14, 29]. Their possible intimate connection should be further examined in  $(\text{Sr}_{1-x}\text{La}_x)_3\text{Ir}_2\text{O}_7$  [22]. On the other hand, strong spin-orbit coupling in iridates is responsible for the conceived formation of an effective  $J = 1/2$  band from a mixture of three  $t_{2g}$  orbitals. It uniquely enables a putative Mott transition to take place on this band without the need of a strong on-site

Coulomb repulsion [15–18]. It has been proposed that a large inter-orbital charge transfer with negative  $\frac{\partial n}{\partial \mu}$  is feasible in a multi-band model with at least one band being close to a Mott transition [12]. To what extent the strong spin-orbit and/or multi-orbital nature of all associated correlated states is relevant to their nontrivial doping-dependent motion is another issue that has to be addressed in order to understand the microscopic driving force for the negative  $\frac{\partial n}{\partial \mu}$  in  $(\text{Sr}_{1-x}\text{La}_x)_3\text{Ir}_2\text{O}_7$ .

Our finding suggests that the quasi-3D electron system in metallic  $(\text{Sr}_{1-x}\text{La}_x)_3\text{Ir}_2\text{O}_7$  likely represents the first experimental case of negative  $\varkappa_e$  in three dimensions, which has been discussed in theory [12, 30] as an important complement to the lower-dimensional cases found in the conventional [6, 7] or oxide [8] semiconductor heterojunctions, monolayer [9] and bilayer [10] graphene, and carbon nanotubes [11]. Those cases were established mainly by two probes for  $\varkappa_e$  via the quantum capacitance [6, 8, 9, 11] and electric field penetration [7, 8], both proportional to  $\frac{\partial n}{\partial \mu}$ . Applying them to study  $(\text{Sr}_{1-x}\text{La}_x)_3\text{Ir}_2\text{O}_7$  is certainly an important task, yet it is non-trivial with single-crystal samples. The difficulty lies in its relatively low value of  $|\frac{\partial n}{\partial \mu}|$  ( $= 5.7 \times 10^{18} \text{ meV}^{-1} \cdot \text{cm}^{-3}$ ) deduced from ARPES, the requirement on surface flatness and/or thickness in the nanoscale for related device fabrications, and the need to tune carrier concentration during measurement. For this, it would be more promising to work with thin-film samples, which, unfortunately, have not yet been grown.

We have presented experimental evidence for a new route toward realizing negative  $\varkappa_e$  via a dominance of the correlation energy, instead of the exchange energy that dominates in all other known cases of negative  $\varkappa_e$  [6–11]. As initially proposed in theory [12], such a route could in principle apply to many correlated materials. The potentially important roles of strong spin-orbit coupling and multi-orbital participation that had not been adequately considered, might provide new perspectives for a more complete theoretical understanding of the negative  $\varkappa_e$  phenomena, as well as a good motive for future surveys on other spin-orbit and/or multi-band correlated metals, such as doped transition-metal oxides or dichalcogenides.

Discovery of bulk materials with negative  $\varkappa_e$  would lead to unique possibilities for related research and applications. According to the compressibility sum rule [30], a negative  $\varkappa_e$  leads to a negative dielectric constant near zero frequency. The bulk nature of these materials would thus allow for RF-optical study of their  $\varkappa_e$ , as well as their applications in metamaterials as active components, neither being possible for their lower-dimensional

counterparts. Use of metal electrodes with negative quantum capacitance in transistors can effectively enhance their gate capacitances, presenting an alternative to the use of “high- $\kappa$ ” dielectric for miniaturization of devices that switch at low voltage with minimal gate-to-channel leakage [8]. Compared with two-dimensional electron/hole systems [6–8], doped correlated metals are typically associated with a high correlation energy scale (on the order of 100 meV) [13]; due to their 3D bulk nature, they are amenable to changes of environment as well as deposition onto any substrate, creating devices with working resistance tunable by film thickness. Application of these materials with negative  $\kappa_e$  in transistors thus promises a good adaptability to the existing CMOS architecture, and could potentially enable room-temperature (field independent) and variable-frequency device operation.

## Methods

Single crystals of  $(\text{Sr}_{1-x}\text{La}_x)_3\text{Ir}_2\text{O}_7$  with different  $x$  were grown by flux techniques similar to earlier reports[19, 23]. Samples were cleaved at 30 K in ultrahigh vacuum prior to ARPES measurements. The presented ARPES results were mostly obtained at 30 K from Beamline 5-4 of the Stanford Synchrotron Radiation Lightsource (SSRL) of SLAC National Accelerator Laboratory using 25 eV photons with a total energy resolution of  $\sim 9$  meV and a base pressure better than  $3 \times 10^{-11}$  Torr. Stability of the photon energy and energy position of the system chemical potential was constantly monitored by measuring a polycrystalline Au sample in direct electrical contact with the sample under study, which showed a typical variation  $< \pm 1$  meV during the measurement on each sample. Fermi surface maps shown resulted from an integration within  $\pm 10$  meV about the chemical potential. A preliminary experiment was performed on  $x = 0.08$  at Beamline 9 A of the Hiroshima Synchrotron Radiation Center (HSRC). Core-level measurements were performed at Beamline 10 of the Advanced Light Source (ALS) at Lawrence Berkeley National Laboratory using 150 eV photons with a total energy resolution of 50 meV at 30 K.

First-principles calculations were performed in a similar way to Ref. [22] using the Vienna Ab initio Simulation Package (VASP). The core and valence electrons were described by the projector augmented wave (PAW) and a plane wave basis, respectively. Exchange-correlation effects were treated using the generalized gradient approximation (GGA). A  $\sqrt{2} \times \sqrt{2}$  superlattice was used with an in-plane lattice constant  $a \sim 3.9 \text{ \AA}$ , due

to a  $12^\circ$ -rotation of the oxygen octahedra surrounding the Ir atoms. Antiferromagnetic order, when present, does not further change the size of the unit cell. Electron-electron interaction between the correlated  $d$  electrons on Ir atoms was included at the GGA+U (on-site Coulomb repulsion) mean-field level. In order to simulate the experimental results shown in Fig. 1, we set  $U = 1.1$  eV and spin-orbit coupling to 2 eV (which is twice the value obtained in the self-consistent computation).

**Acknowledgement** We thank K. S. Burch, T.-R. Chang, Y.-H. Chu, Z. Hussain, H. Lin, V. Madhavan, Z.-X. Shen, Z.-Y. Weng, and H. Yao for discussions. The work at Boston College was supported by a startup fund (J.H., R.-H.H.), the US NSF CAREER Award DMR-1056625 (T.H., C.D., X.C., S.D.W.), NSF Graduate Research Fellowship GRFP-5100141 (T.R.M.), DOE-DE-SC0002554 (Z.W.), and W. M. Keck Foundation (M.J.N.). The work at NEU was supported by the DOE, BES Contract No. DE-FG02-07ER46352, and benefited from NEU’s ASCC, theory support at the ALS and the allocation of supercomputer time at NERSC through DOE grant DE-AC02-05CH11231. ARPES experiments were performed at the SSRL and the ALS, supported respectively by the US DOE, BES Contract Nos. DE-AC02-76SF00515 and DE-AC02-05CH11231, and at HSRC with the approval of Proposal No. 14-A-1.

**Competing Interests** The authors declare that they have no competing financial interests.

**Author Contributions** J.H. and T.H. contribute equally to this work. J.H. and R.-H.H. proposed and designed the research. J.H. and T.R.M. carried out the ARPES measurements with the help from Y.H., S.-K.M., Y.Z., Q.L. and H.P.. T.H., C.D. and X.C. grew the samples. T.H., J.H. and T.R.M. characterized the samples with the EDS. H.H. and R.S.M. performed the first-principles calculations and, along with K.K., provided theoretical guidance. M.H., D.H.L., S.-K.M., M.A. and K.S. maintained the experimental facilities. J.H. analyzed the data. J.H. and R.-H.H. wrote the paper with key inputs from Z.W., Y.H., S.D.W., A.B., and R.S.M.. R.-H.H., S.D.W., A.B. and M.J.N. are responsible for project direction, planning and infrastructure.

**Correspondence** Supplementary information is available in the online version of the



paper. Reprints and permissions information is available online. Correspondence and requests for materials should be addressed to R.-H.H..

- 
- [1] Baughman, R. H., Stafström, S., Cui, C. & Dantas, S. O. Materials with negative compressibilities in one or more dimensions. *Science* **279**, 1522-1524 (1998).
  - [2] Lakes, R. S., Lee, T., Bersie, A. & Wang, Y. C. Extreme damping in composite materials with negative-stiffness inclusions. *Nature* **410**, 565-567 (2001).
  - [3] Jaglinski, T., Kochmann, D., Stone, D. & Lakes, R. S. Composite materials with viscoelastic stiffness greater than diamond. *Science* **315**, 620-622 (2007).
  - [4] Liu, Z. *et al.* P. Locally resonant sonic materials. *Science* **289**, 1734-1736 (2000).
  - [5] Fang, N. *et al.* Ultrasonic metamaterials with negative modulus. *Nature Mater.* **5**, 452-456 (2006).
  - [6] Kravchenko, S. V., Rinberg, D. A., Semenchinsky, S. G., Pudalov, V. M. Evidence for the influence of electron-electron interaction on the chemical potential of the two-dimensional electron gas. *Phys. Rev. B* **42**, 3741-3744 (1990).
  - [7] Eisenstein, J. P., Pfeiffer, L. N., West, K. W. Negative compressibility of interacting two-dimensional electron and quasiparticle gases. *Phys. Rev. Lett.* **68**, 674-677 (1992).
  - [8] Li, L. *et al.* Very Large Capacitance Enhancement in a Two-Dimensional Electron System. *Science* **332**, 825-828 (2011).
  - [9] Yu, G. L. *et al.* Interaction phenomena in graphene seen through quantum capacitance. *Proc. Natl. Acad. Sci.* **110**, 3282-3286 (2013).
  - [10] Lee, K. *et al.* Chemical potential and quantum Hall ferromagnetism in bilayer graphene. *Science* **345**, 58-61 (2014).
  - [11] Ilani, S., Donev, L. A. K., Kindermann, M. & McEuen, P. L. Measurement of the quantum capacitance of interacting electrons in carbon nanotubes. *Nature Phys.* **2**, 687-691 (2006).
  - [12] Kopp, T. & Mannhart, J. Calculation of the capacitances of conductors: Perspectives for the optimization of electronic devices. *J. App. Phys.* **106**, 064504 (2009).
  - [13] Imada, M., Fujimori, A. & Tokura, Y. Metal-insulator transitions. *Rev. Mod. Phys.* **70**, 1039 (1998).

- [14] Fujimori, A. *et al.* Core-level photoemission measurements of the chemical potential shift as a probe of correlated electron systems. *J. Electron. Spectrosc. Relat. Phenom.* **124**, 127-138 (2002).
- [15] Kim, B. J. *et al.* Novel  $J_{eff}=1/2$  Mott State Induced by Relativistic Spin-Orbit Coupling in  $\text{Sr}_2\text{IrO}_4$ . *Phys. Rev. Lett.* **101**, 076402 (2008).
- [16] Moon, S. J. *et al.* Dimensionality-controlled insulator-metal transition and correlated metallic state in 5d transition metal oxides  $\text{Sr}_{n+1}\text{Ir}_n\text{O}_{3n+1}$  ( $n = 1, 2, \text{and } \infty$ ). *Phys. Rev. Lett.* **101**, 226402 (2008).
- [17] Ishii, K. *et al.* Momentum-resolved electronic excitations in the Mott insulator  $\text{Sr}_2\text{IrO}_4$  studied by resonant inelastic x-ray scattering. *Phys. Rev. B* **83**, 115121 (2011).
- [18] Arita, R., Kunes, J., Kozhevnikov, A. V., Eguluz, A. G. & Imada, M. Ab initio Studies on the Interplay between Spin-Orbit Interaction and Coulomb Correlation in  $\text{Sr}_2\text{IrO}_4$  and  $\text{Ba}_2\text{IrO}_4$ . *Phys. Rev. Lett.* **108**, 086403 (2012).
- [19] Li, L. *et al.* Tuning the  $J_{eff} = 1/2$  insulating state via electron doping and pressure in the double-layered iridate  $\text{Sr}_3\text{Ir}_2\text{O}_7$ . *Phys. Rev. B* **87**, 235127 (2013).
- [20] Wang, Q. *et al.* Dimensionality-controlled Mott transition and correlation effects in single-layer and bilayer perovskite iridates. *Phys. Rev. B* **87**, 245109 (2013).
- [21] King, P. D. C. *et al.* Spectroscopic indications of polaronic behavior of the strong spin-orbit insulator  $\text{Sr}_3\text{Ir}_2\text{O}_7$ . *Phys. Rev. B* **87**, 241106 (2013).
- [22] Okada, Y. *et al.* Imaging the evolution of metallic states in a correlated iridate. *Nature Mater.* **12**, 707-713 (2013).
- [23] Dhital, C. *et al.* Spin ordering and electronic texture in the bilayer iridate  $\text{Sr}_3\text{Ir}_2\text{O}_7$ . *Phys. Rev. B* **86**, 100401(R) (2012).
- [24] Shen, K. M. *et al.* Missing Quasiparticles and the Chemical Potential Puzzle in the Doping Evolution of the Cuprate Superconductors. *Phys. Rev. Lett.* **93**, 267002 (2004).
- [25] Yagi, H. *et al.* Chemical potential shift in lightly doped to optimally doped  $\text{Ca}_{2-x}\text{Na}_x\text{CuO}_2\text{Cl}_2$ . *Phys. Rev. B* **73**, 172503 (2006).
- [26] Lee, J. S., Krockenberger, Y., Takahashi, K. S., Kawasaki, M. & Tokura, Y. Insulator-metal transition driven by change of doping and spin-orbit interaction in  $\text{Sr}_2\text{IrO}_4$ . *Phys. Rev. B* **85**, 035101 (2012).
- [27] Armitage, N. P., Fournier, P. & Greene, R. L. Progress and perspectives on electron-doped

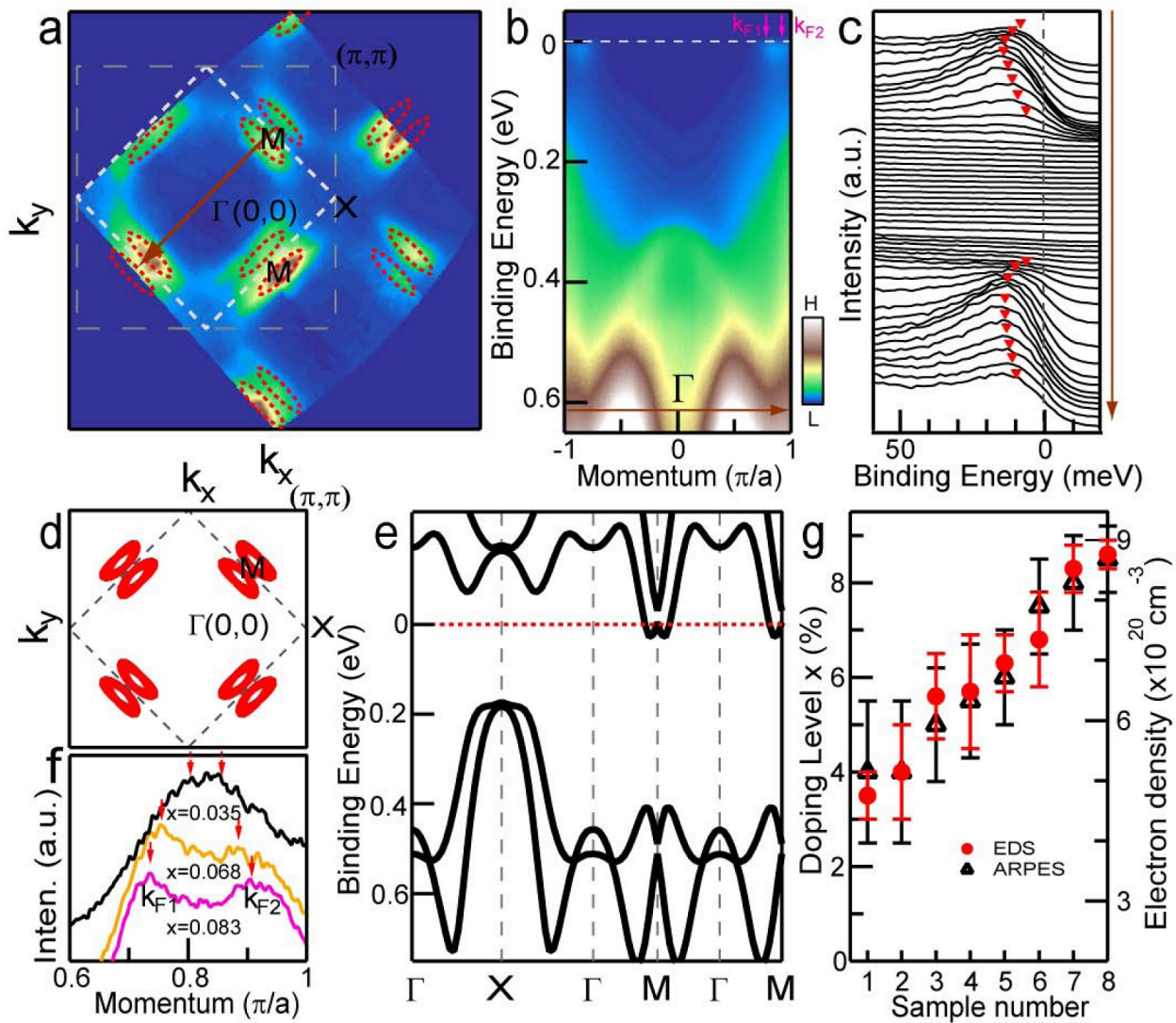
- cuprates. *Rev. Mod. Phys.* **82**, 2421 (2010).
- [28] Das, T., Markiewicz, R. S. & Bansil, A. Strong correlation effects and optical conductivity in electron-doped cuprates. *EPL* **96** 27004 (2011).
- [29] Veillette, M., Bazaliy, Y. B., Berlinsky, A. J., & Kallin, C. Stripe Formation by Long Range Interactions within SO(5) Theory. *Phys. Rev. Lett.* **93**, 267002 (2004).
- [30] Li, Q., Hwang, E. H., & Das Sarma, S. Temperature-dependent compressibility in graphene and two-dimensional systems. *Phys. Rev. B* **84**, 235407 (2011).

FIG. 1: **Fermi surface and electronic band structure of  $(\text{Sr}_{1-x}\text{La}_x)_3\text{Ir}_2\text{O}_7$  with  $x = 0.057$ .** **a**, Fermi surface map featuring four electron Fermi pockets near M points, as eyeguided by the red dashed ellipses. **b**, Band dispersion along the high-symmetry direction indicated by the brown arrow in **a**, revealing two electron-like bands close to the chemical potential (zero binding energy). **c**, Energy distribution curves (EDCs) for **b**, showing the electron-like bands at low energy marked by red triangles. Fermi surface (**d**) and band dispersions along high-symmetry directions (**e**), given by first-principles calculation. Note the overall agreement between the calculation and experiment modulo the need of a proper renormalization factor. **f**, Momentum distribution curves at the chemical potential for selected  $x$ , showing peaks at positions marked as  $k_{F1}$  and  $k_{F2}$  (also in **b**). **g**, La substitution (or doping) level and the corresponding electron density determined by the EDS (red circles) and ARPES (black triangles) on all samples studied. The error bars result from the spatial variation on a given sample surface (for EDS) and uncertainty in determining Fermi momenta of the conduction band (for ARPES).

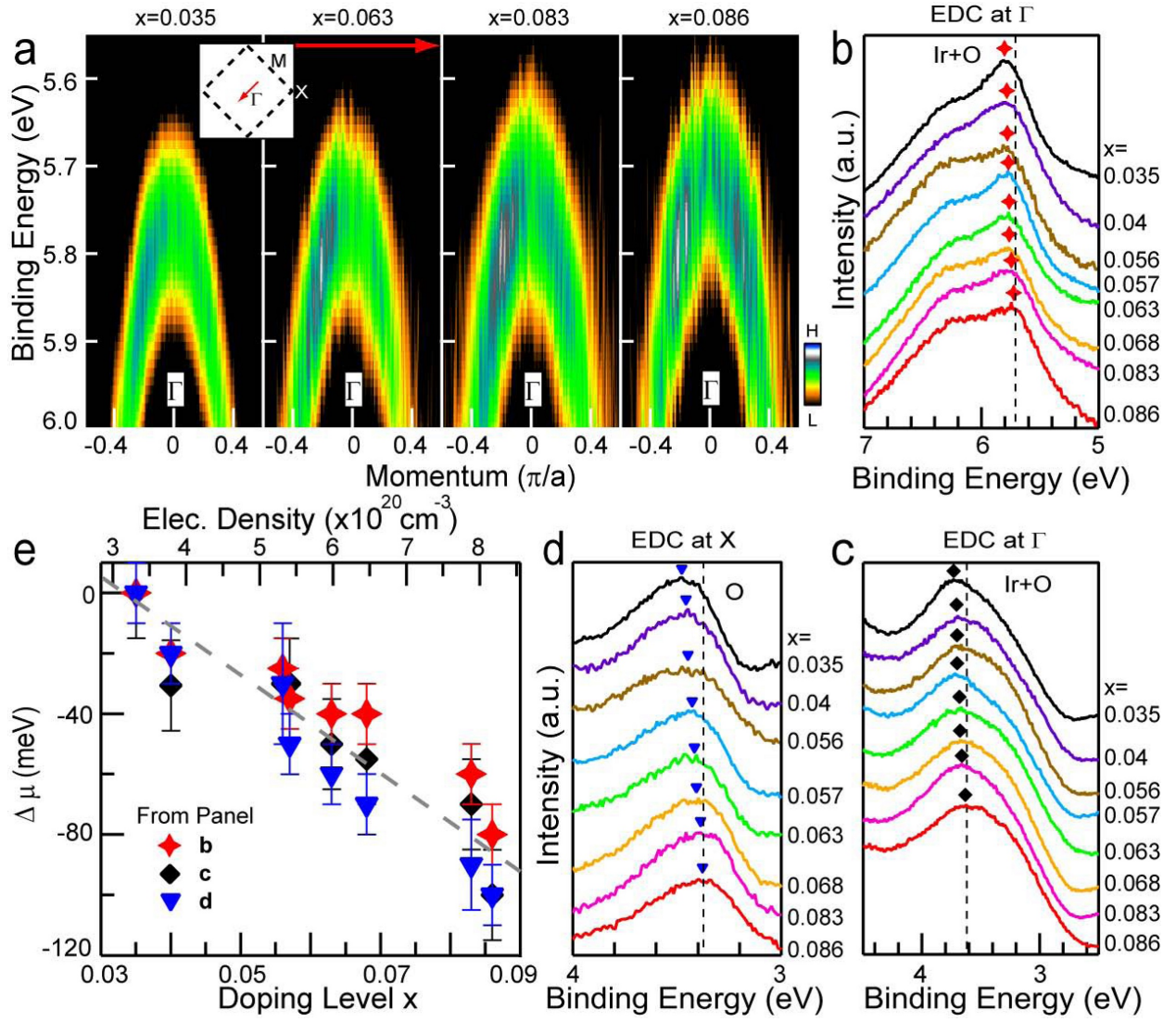
FIG. 2: **Chemical potential shift upon electron doping in  $(\text{Sr}_{1-x}\text{La}_x)_3\text{Ir}_2\text{O}_7$ .** **a**, Band dispersions along the red arrow (inset) in the deep valence region around  $\Gamma$  point for selected  $x$ . Second derivative with respect to energy has been taken on the raw data to enhance the spectral contrast. **b** & **c**, EDCs at  $\Gamma$  point shown in two energy ranges for all  $x$ . Symbols point out spectral peaks for states of a mixed Ir-O character, with the one in **b** corresponding to the same states shown in **a**. **d**, EDCs at X point for states of a O  $2p$  character. See Supplementary Fig. S1 for the orbital character assignments of states based on first-principles calculations. **e**, Chemical potential shift as a function of  $x$  (and the calculated electron density), deduced from the states as marked correspondingly in **b-d**. For convenience,  $\mu$  of  $x = 0.035$  is set as a zero reference. The error bars reflect the uncertainty in determining the energy position of the raw EDC peak or centroid.

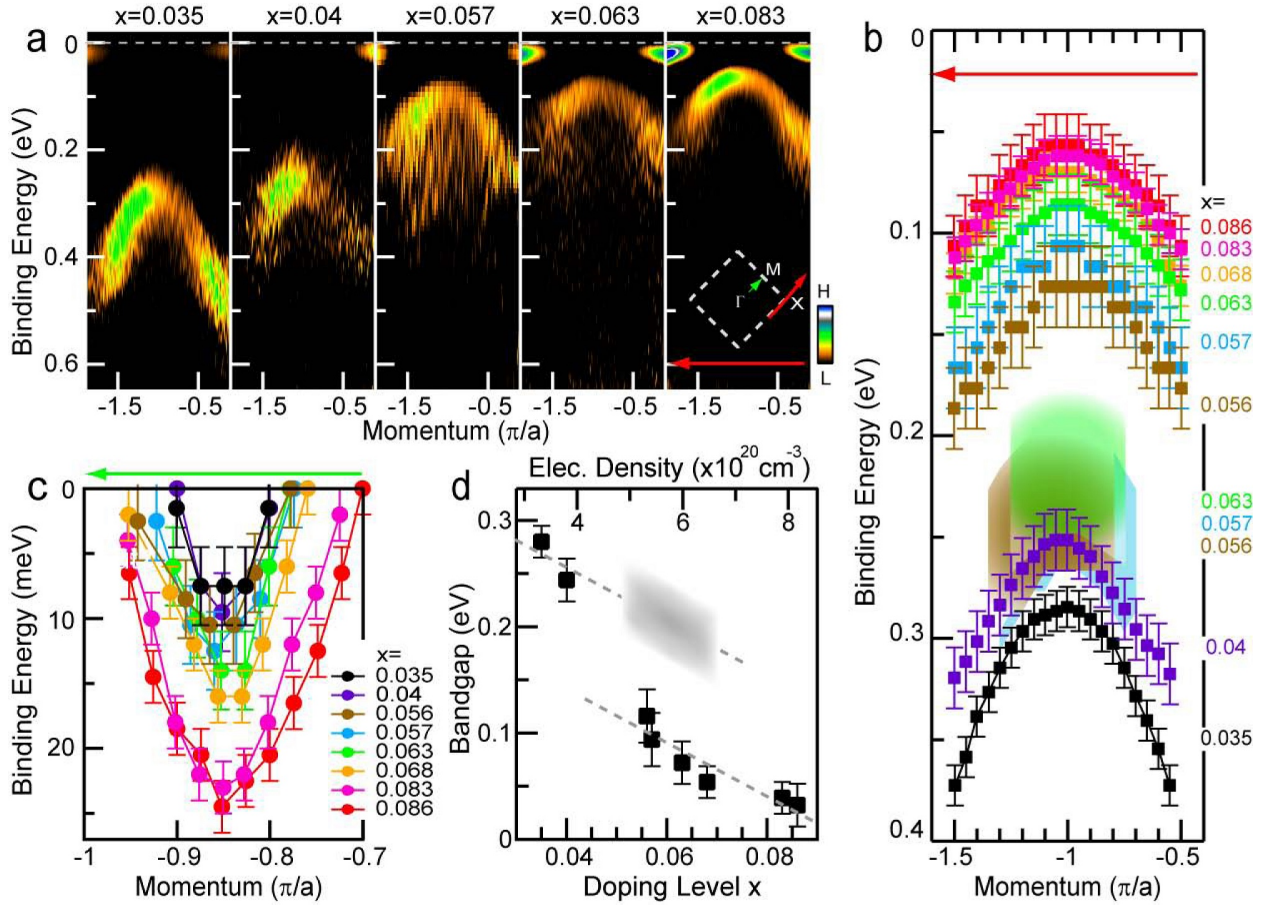
**FIG. 3: Doping evolutions of the valence band top at X point and the conduction band bottom near M point of  $(\text{Sr}_{1-x}\text{La}_x)_3\text{Ir}_2\text{O}_7$ .** **a**, Band dispersions (second derivative) of the low-lying valence band along the red arrow (inset) for selected  $x$ . Note a more diffuse intensity distribution at  $x \sim 0.057$  due to the presence of multiple spectral features (see below). See Supplementary Fig. S3 for raw EDCs. Doping evolution of the low-lying valence band (**b**) and conduction band (**c**) dispersions along, respectively, the red and green arrows shown in the inset of **a**, which were extracted by tracking the second-derivative EDC peaks. Composite line shapes seen in the valence band at  $x = 0.056, 0.057$  &  $0.063$  are better understood as composed of multiple features with one dominant component at high energy and another at low energy, as exemplified in Fig. 4b for EDCs at X point. **d**, Doping evolution of the indirect bandgap between the valence band top and the conduction band bottom. The valence band top is defined by the dominant second-derivative feature of the valence band in **a**, which changes character across  $x \sim 0.057$ . The bandgap has thus a different nature at lower and higher  $x$  and displays evolutions as guided by the dashed lines. Grey shaded area denotes the bandgap vaguely defined by the high-energy feature of the valence band at  $x \sim 0.057$ . See Fig. 4b and related discussions in text. All error bars reflect the uncertainty in determining the energy position of the second-derivative EDC peak.

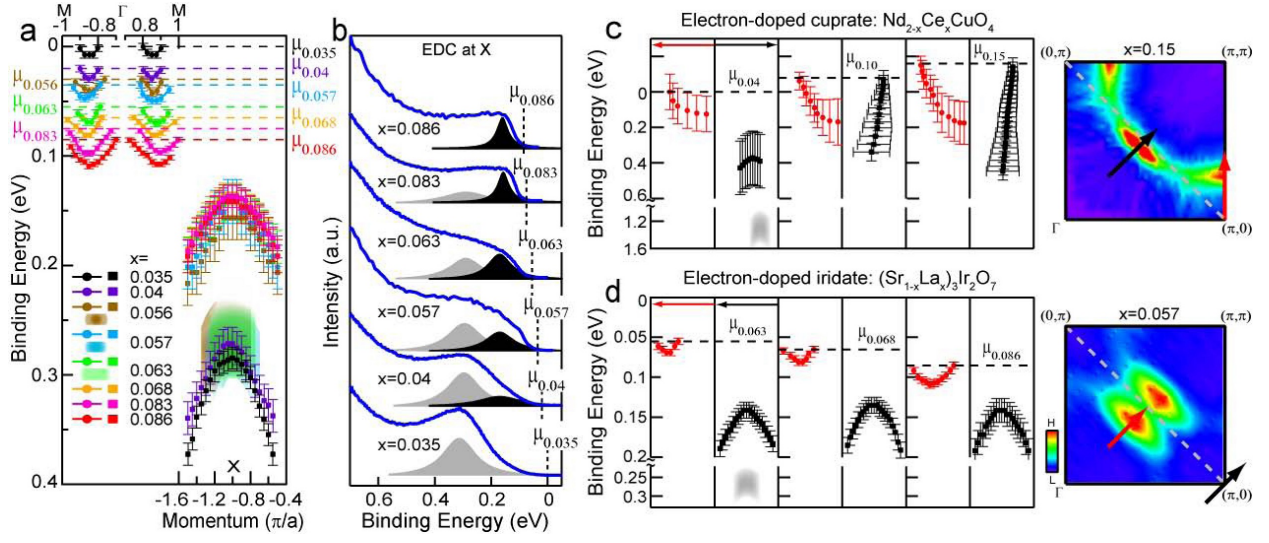
**FIG. 4: Doping evolution of the low-lying band structure of  $(\text{Sr}_{1-x}\text{La}_x)_3\text{Ir}_2\text{O}_7$  and its comparison with  $\text{Nd}_{2-x}\text{Ce}_x\text{CuO}_4$ .** **a**, Extracted dispersions of the conduction band near M point and the low-lying valence band around X point for all  $x$ , plotted on a common energy scale relative to the energy positions of their respective chemical potentials. The chemical potential of  $x = 0.035$  is set to be zero and the relative shifts of chemical potential are obtained from Fig. 2e. **b**, EDCs at X point for selected  $x$ . The grey and black peaks serve as eyeguides only for, respectively, the dominant states that define the valence band top at  $x < 0.056$  and  $x \geq 0.056$ , with a spectral weight transfer between them. Spectra are plotted in the same energy scale as in **a**. See Supplementary Fig. S3 for the raw spectra. **c** & **d**, Doping evolutions of the conduction band, the low-lying valence band and the relative chemical potential for  $\text{Nd}_{2-x}\text{Ce}_x\text{CuO}_4$  (reproduced from Refs. [14, 27]) &  $(\text{Sr}_{1-x}\text{La}_x)_3\text{Ir}_2\text{O}_7$  (this work), respectively. The chemical potential of  $\text{Nd}_{2-x}\text{Ce}_x\text{CuO}_4$  was measured by referencing to different core levels. Note that the conduction (red) and valence (black) bands are located at different momentum locations as sampled along the arrows shown in the respective (symmetrized) Fermi surface maps of both materials. The error bars in **a**, **d** & **c** are reproduced, respectively, from those in Fig. 3b & c, and in Ref. [27].











***Supplementary information for***  
**Spectroscopic evidence for negative electronic compressibility in a quasi-three-dimensional spin-orbit correlated metal**

**Supplementary Discussion 1: Remark on the energy shift of core levels and deep valence bands**

In core level measurements, the binding energy shift  $\Delta E$  relative to chemical potential  $\mu$  is determined by several key energy terms [1], i.e.,  $\Delta E = \Delta\mu + K\Delta Q + \Delta V_M + \Delta E_R$ , where  $\Delta\mu$  is the change in chemical potential;  $\Delta Q$  is the change in the number of valence electrons on the atom,  $K$  is a constant, and  $K\Delta Q$  is called the chemical shift;  $\Delta V_M$  is the change in Madelung potential; and  $\Delta E_R$  is the change in the screening of core hole. On the other hand, the energy shifts of the fully occupied yet delocalized (valence) band-like states at low energy were suggested to simply represent  $\Delta\mu$  [2]. The effectiveness of this valence-band approach is attributed to the consideration that the effects due to the  $K\Delta Q$ ,  $\Delta V_M$  and  $\Delta E_R$  terms, which are site-dependent and/or local, can be averaged out due to the delocalized nature of the deep valence states. Its agreement with the core-level approach was later demonstrated in a detailed study on the same material [3].

Here we confirm that the  $K\Delta Q$ ,  $\Delta V_M$  and  $\Delta E_R$  terms have little contribution to the energy shifts of the delocalized deep valence band states in  $(\text{Sr}_{1-x}\text{La}_x)_3\text{Ir}_2\text{O}_7$ . First, core-level measurements on both electron- and hole-doped cuprates showed that the Cu and O states in the  $\text{CuO}_2$  plane shift in opposite directions upon doping where  $K\Delta Q$  is sizeable [1]. This contrasts with our observation of a similar shift on both the Ir and O states in the  $\text{IrO}_2$  plane (Main Fig. 2e). Second,  $\Delta V_M$  is of an opposite sign for the anion and cation states, again different from our observation on Ir and O. Third, the screening of core or valence hole by conduction electrons is expected to be much stronger for states in the metallic  $\text{IrO}_2$  plane than the insulating Sr-O charge reservoir layer. Because the O states at X point contain substantial contributions from both in and out of the  $\text{IrO}_2$  plane, their overall energy shift should be weaker than that of the Ir states of a pure in-plane character, provided a large  $\Delta E_R$ . Besides, the Sr states should show a much weaker (if any) doping-dependent energy shift due to screening, compared to the Ir states. Neither of these expectations are consistent with our observations (see Main Fig. 2e and Fig. S2c, respectively).

We have also studied the energy shifts of the Ir 4*f* and Sr 3*d* core levels in  $(\text{Sr}_{1-x}\text{La}_x)_3\text{Ir}_2\text{O}_7$  at selected  $x$ . The results are qualitatively consistent with those for the deep valence band states (Fig. S2). The much increased error bars in these shifts (compared to those in Main Fig. 2e) are due to a poor energy resolution (50 meV) of the core level measurement [4] and the broad inherent width of the core level peaks. This uncertainty, together with the lack of doping levels studied and the possibility that other energy terms may have a weak yet non-vanishing contribution to the core level shift, preclude a quantitative comparison with the deep valence band shifts. Nevertheless, both core level states studied exhibit a lowering of binding energy as  $x$  increase, which qualitatively resembles those of the deep valence band. This consistency further supports our conclusion that the chemical potential decreases with electron doping in  $(\text{Sr}_{1-x}\text{La}_x)_3\text{Ir}_2\text{O}_7$ .

## **Supplementary Discussion 2: Effect of possible variation of the sample work function**

Work function is the energy difference between the vacuum level and chemical potential of materials. It is possible that the work function of  $(\text{Sr}_{1-x}\text{La}_x)_3\text{Ir}_2\text{O}_7$  varies with  $x$ . However, the binding energy of electronic states measured by ARPES is independent of the work function of the sample itself, which is given by  $E_B = \hbar\omega - E_K - \Phi_A$ , where  $\hbar\omega$  is the energy of the incident photon and  $\Phi_A$  is the work function of the photoelectron analyzer. As illustrated in Fig. S4, the chemical potentials ( $E_F$ ) of the sample and the analyzer are aligned when they are electrically connected in experiment. Because of the possible difference in their work functions, there exists an electric field between the sample and the analyzer which accelerates or decelerates the photoelectrons. As a result, the kinetic energy ( $E_k$ ) of these photoelectrons measured by the detector in the analyzer is typically different from that of the same photoelectrons right emitted from the sample surface ( $E'_k$ ). For the photoemission from some given states, change in the sample work function  $\Phi_S$  with a fixed sample chemical potential would result in a change in  $E'_k$ , but not  $E_k$ , i.e., there would be no energy shift of

the states measured by ARPES.

---

- [1] Fujimori, A. *et al.* Core-level photoemission measurements of the chemical potential shift as a probe of correlated electron systems. *J. Electron. Spectrosc. Relat. Phenom.* **124**, 127-138 (2002).
- [2] Shen, K. M. *et al.* Missing Quasiparticles and the Chemical Potential Puzzle in the Doping Evolution of the Cuprate Superconductors. *Phys. Rev. Lett.* **93**, 267002 (2004).
- [3] Yagi, H. *et al.* Chemical potential shift in lightly doped to optimally doped  $\text{Ca}_{2-x}\text{Na}_x\text{CuO}_2\text{Cl}_2$ . *Phys. Rev. B* **73**, 172503 (2006).
- [4] The fact that a clear energy variation of spectral features can be measured with an energy resolution of the same order is not too surprising, as it has been experimentally demonstrated that a  $\pm 40$  meV binding energy shift could be measured with an energy resolution  $\sim 1$  eV, given a good statistic of the spectra [5].
- [5] Ino, A. *et al.* Chemical potential shift in overdoped and underdoped  $\text{La}_{2-x}\text{Sr}_x\text{CuO}_4$ . *Phys. Rev. Lett.* **79**, 2101-2104 (1997).
- [6] King, P. D. C. *et al.* Spectroscopic indications of polaronic behavior of the strong spin-orbit insulator  $\text{Sr}_3\text{Ir}_2\text{O}_7$ . *Phys. Rev. B* **87**, 241106 (2013).
- [7] Jozwiak, C. M. Thesis: A new spin on photoemission spectroscopy. (2005).



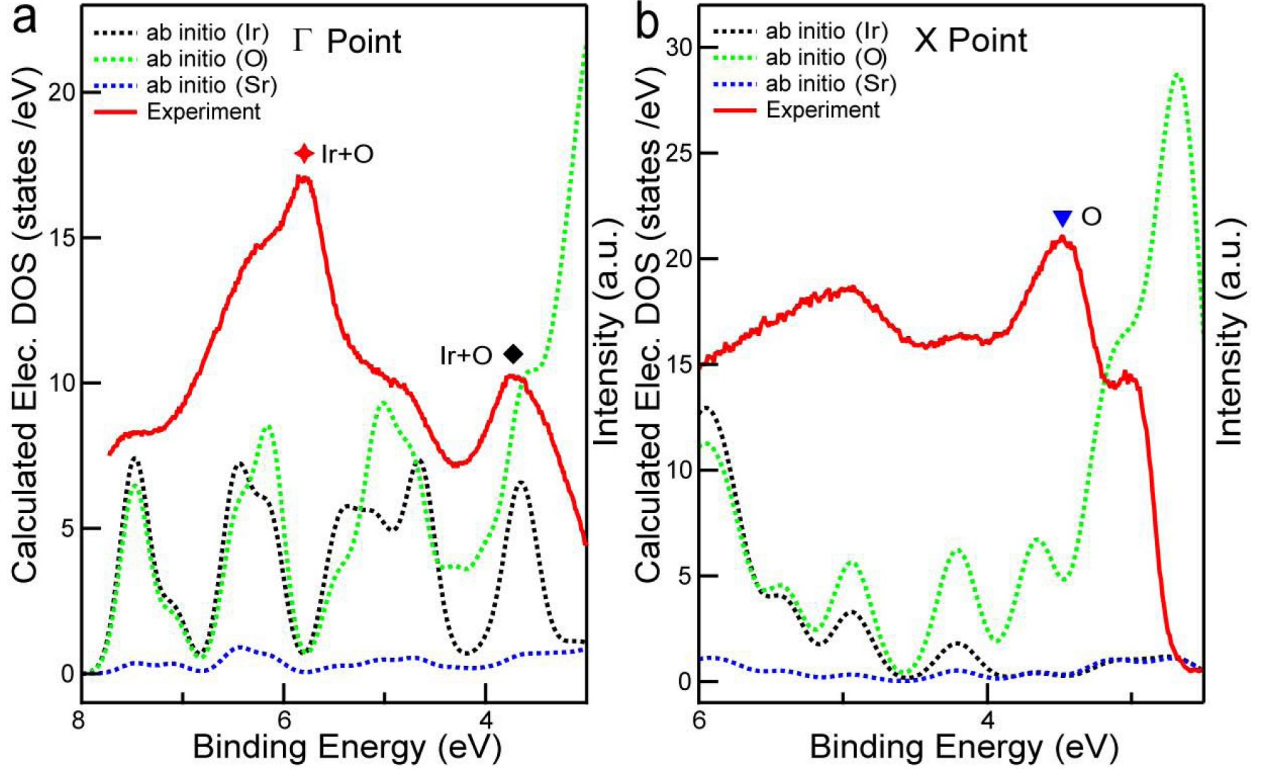


Fig. S 1: **Determination of the orbital characters of the interested deep valence band states.** **a & b**, Comparison of the orbital-specific partial density of states from the first-principles calculation with the experimental EDCs for  $x = 0.035$  at  $\Gamma$  and X points, respectively. The chemical potential is set in the calculation such that the Fermi surface volume of the conducting band agrees with the experimental value. Note, however, that the calculated bands may differ from the experiment in energy by some proper renormalization factors (cf. Main Fig. 1b & e). Because of this, disagreements exist between the experiment and calculation in terms of the line shapes and precise energy positions of band features as seen here. Nevertheless, the comparison still allows us to deduce that the two EDC peaks seen at  $\Gamma$  point (red star and black diamond) are associated with states of a dual Ir and O character, while the peak at X point (blue triangle) is of a predominantly O content (consistent with Ref. [6]). The observation that all peaks exhibit a similar energy shift with the change of doping (Main Fig. 2e) supports an ascription of these shifts to the shift of chemical potential. See Supplementary Discussion 1 for discussion.

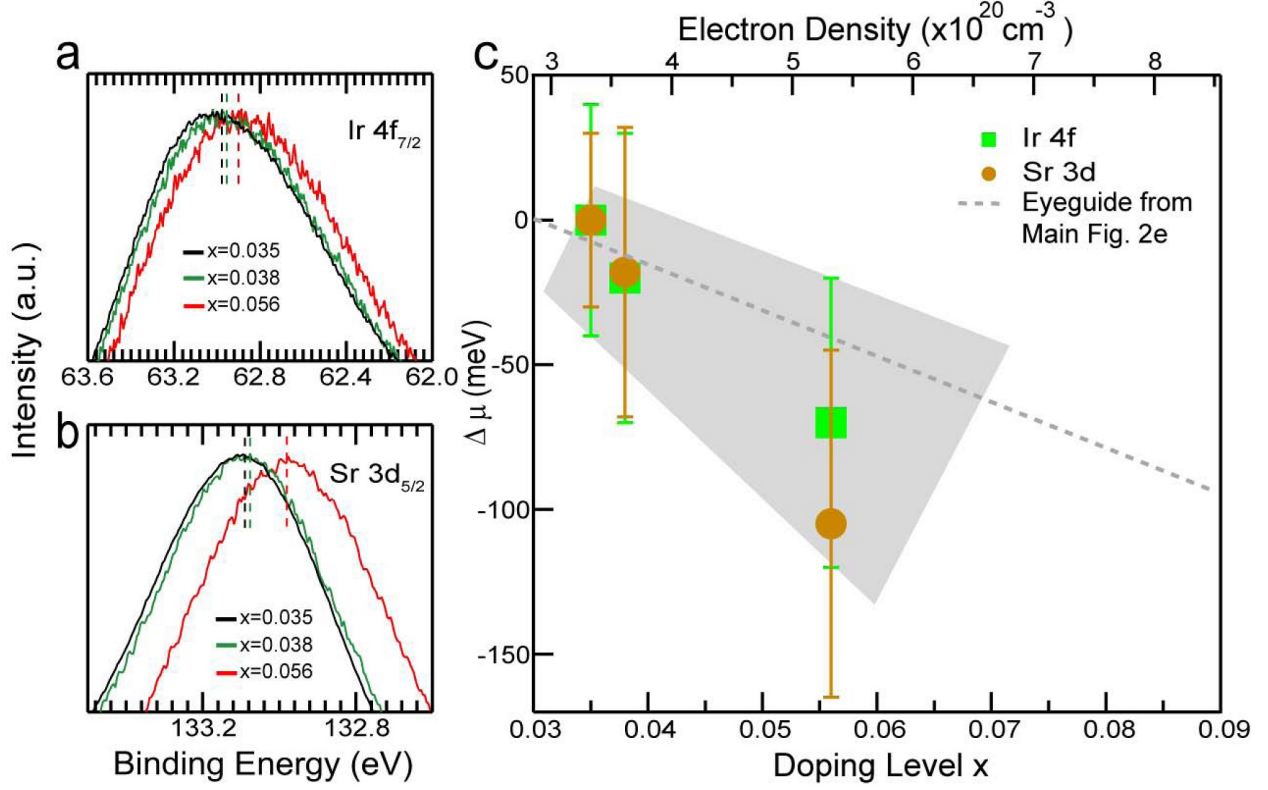


Fig. S 2: **Energy shifts of the Ir 4f and Sr 3d core levels in  $(\text{Sr}_{1-x}\text{La}_x)_3\text{Ir}_2\text{O}_7$  at  $x = 0.035, 0.038$  &  $0.056$ .** **a** & **b**, Ir 4f<sub>7/2</sub> & Sr 3d<sub>5/2</sub>. **c**, Energy shift as a function of  $x$  (and the calculated electron density), extracted from **a** and **b**. For convenience,  $\mu$  of  $x = 0.035$  is set as a zero reference. The error bars reflect the uncertainty in determining the energy position of the raw EDC peak or centroid. Dashed line is the eyeguide reproduced from Main Fig. 2e for the chemical potential shift deduced from the deep valence band shifts.



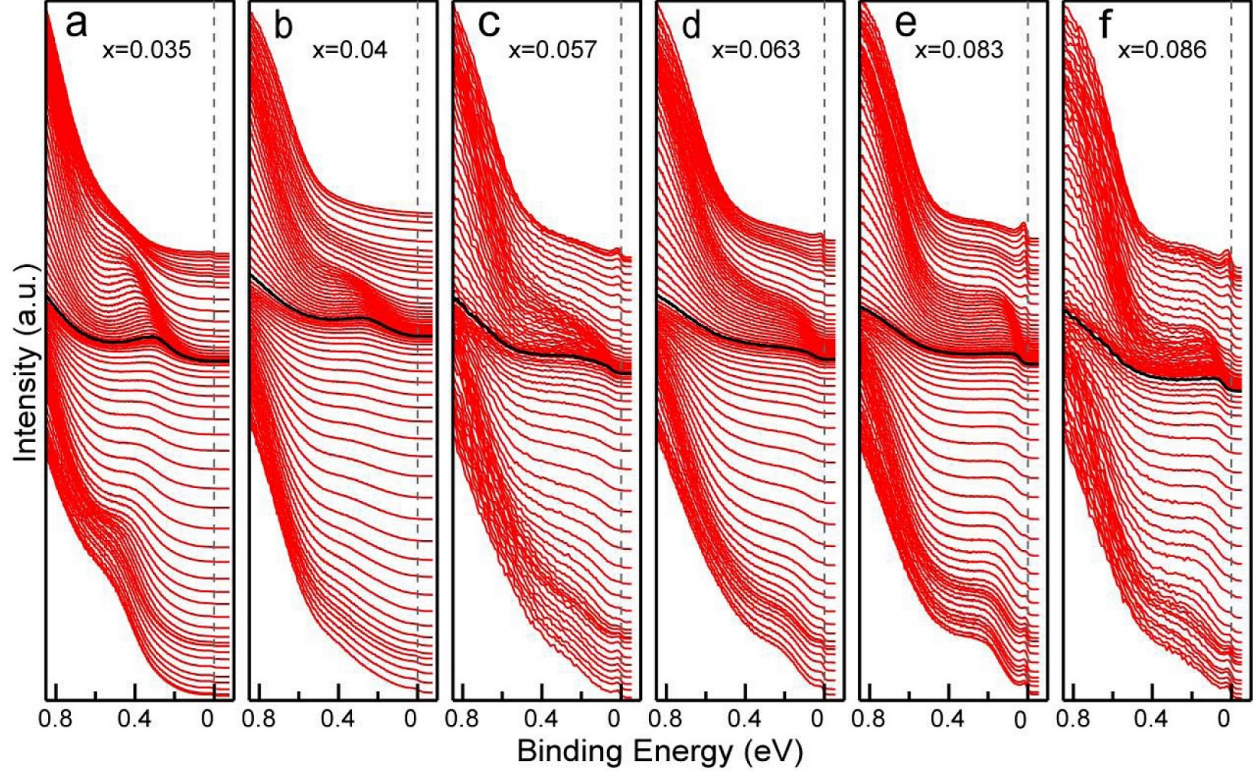


Fig. S 3: **Raw EDCs of the valence band around X point for selected  $x$ .** Data were taken along the red cut shown in the inset of Main Fig. 3a. The black curves are the EDCs at X point, which are reproduced in Main Fig. 4b.

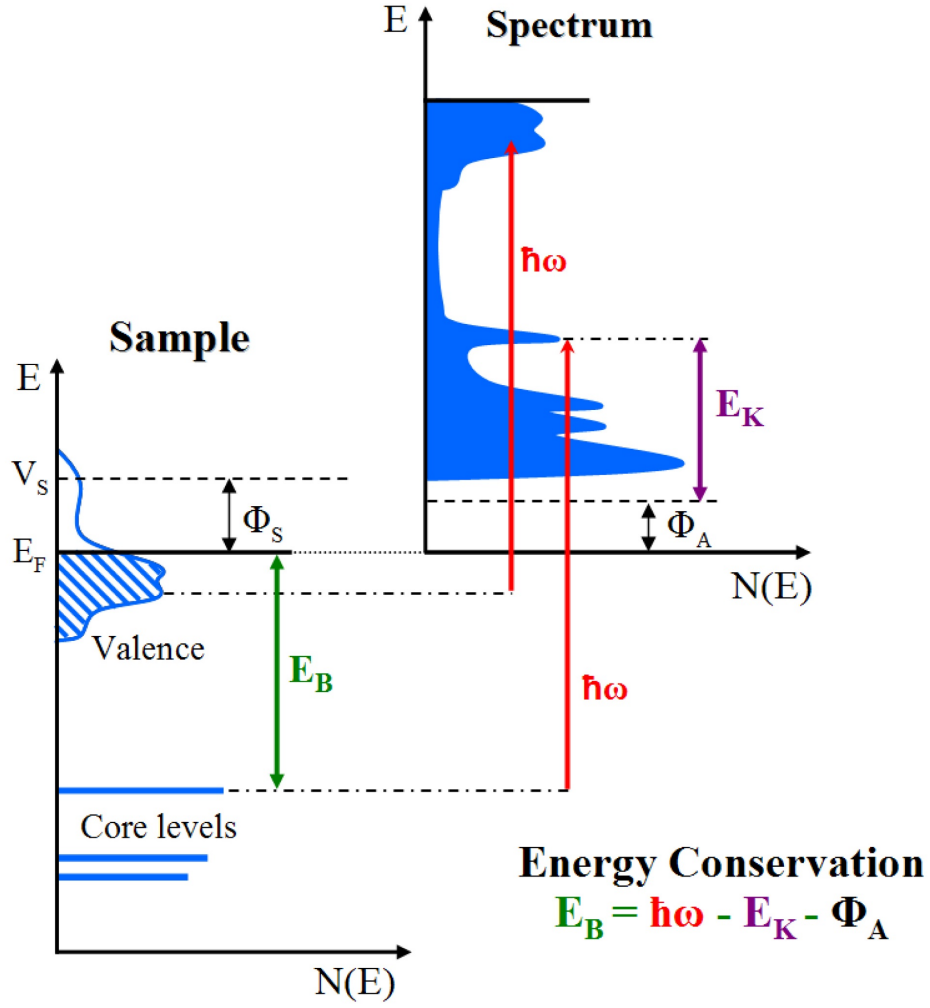


Fig. S 4: **Energetics of the photoemission process.** The electron energy distribution produced by incoming photons with energy  $\hbar\omega$  and measured as a function of the kinetic energy  $E_k$  of the photoelectrons (right) can be expressed in terms of the binding energy  $E_B$  (left) when one refers to the density of states inside the solid ( $E_B = 0$  at  $E_F$ ).  $\Phi_S$  and  $\Phi_A$  are the work functions of the sample and analyzer, respectively. Figure is reproduced from Ref. [7].